19. Line Shapes and Radiation Transfer

The shapes of collisionally broadened atomic lines is a topic almost as old as Fraunhofer's discovery of the existence of discrete lines. *Lorentz* provided the first quantitative theory in 1906 [19.1], and *Weisskopf* advanced this to the *impact theory* by 1933 [19.2]. *Holtsmark* [19.3], *Kuhn* [19.4] and *Margenau* [19.5] meanwhile developed the *quasistatic* or *statistical* theory which describes the line wing, and *Jablonski* put this on a quantum mechanical footing in the context of free–free molecular radiation [19.6]. By the 1940s, satellite bands in the line wings, and a variety of high and low pressure line shapes and broadening rates had been measured. Initial confusion regarding the validity of the contrasting *impact* versus *static* approaches was largely resolved by unified treatments of the Fourier integral theory [19.7–10]. *Baranger* then provided a quantum basis for the impact theory, including level degeneracies [19.11]. Descriptions can be found in a variety of reviews and references therein, including [19.2, 5, 12–16]. The broadening of molecular lines involves the additional complication of rotationally nonadiabatic collisions; this was initially addressed by *Anderson* [19.10] and later with great thoroughness by *van Kranendonk* [19.17]. This chapter and most of the above theories are concerned with neutral atomic gases, which is sometimes called *pressure broadening*. In plasmas, electron, ion, and neutral collisions all contribute to the line shapes and strengths; thus the emitted lines provide a powerful diagnostic of plasma conditions. Neither molecular nor plasma broadening will be covered here; the latter is reviewed in [19.14–16, 18], and in Chapts. 59 and 48.

19.1 Collisional Line Shapes

The neutral-gas theories described above generally used phenomenological or long range forms of the atomic and molecular interactions, and most measurements were not sufficiently detailed to test the validity of these parameterizations or the theoretical approximations. A great deal of the work since mid century has been directed towards obtaining more realistic and accurate descriptions of these interactions and of the full line shapes. In addition, many new types of observations have stimulated variations on the basic theories and descriptions. This includes topics such as collision-induced forbidden transitions, satellite shapes, spectral and polarization redistribution, orientation and alignment effects, Doppler-free spectroscopy and very low temperature collisions. Most of these topics are beyond the scope of this brief and basic description of neutral collisional line shapes.

19.1.1 Voigt Line Shape

An atomic (or molecular or ionic) line has an intrinsic Lorentzian shape that reflects the Fourier transform of the exponentially decaying spontaneous emission. For a spontaneous decay rate Γ, the fullwidth at half maximum (FWHM) is $\Delta\omega = \Gamma$. Due to the Maxwellian distribution of atomic velocities v in a thermal va-

por, and the Doppler shift $\Delta\omega_D = v/\lambda$, the resonance frequencies of atoms in the laboratory frame have a Gaussian distribution. The Doppler width of this distribution is approximately $\omega_0 u/c$, where ω_0 is the resonant frequency and u is the mean thermal velocity. The full line shape is thus a convolution of the natural Lorentzian with the thermal Gaussian; a Voigt profile. In the presence of collisions, the line from each atom broadens, shifts and becomes asymmetric, and this is normally convoluted with the Gaussian velocity distribution to obtain the complete line shape. Collisions may also cause weak or dipole-forbidden transitions to become stronger as well as broader.

19.1.2 Interaction Potentials

Theories of collisional line shapes consider an ensemble average of collisional interactions. For atomic gases, the description of each individual collision or interaction generally starts with a molecular model for a pair of interacting atoms, since the Born–Oppenheimer approximation is appropriate for thermal atomic collisions (electron velocities $\gg$ nuclear velocities) [19.19]. The radiative transition then occurs between adiabatic electronic molecular states that separate to the atomic states of the transition under consideration. The notation $V_u(R)$ denotes the electronic energy of the upper state, and $V_g(R)$ the lower state, where R is the internuclear separation, and the total atomic energies are E_1 and E_0 with $E_1 - E_0 = h\omega_0$ (Fig. 19.1). The next simplification is to assume that the atom-pair statistically branch into adiabatic motion along each of the molecular states associated with the initial atomic state, and radiation to each of the final states is summed independently, assuming they are also completely adiabatic. This ignores an inevitable nonadiabatic coupling between the states as their energy separation decreases to zero at large R, but as discussed below this has been shown to have a very minor effect on line broadening. The single-collision problem then reduces to calculating the spectrum of a molecular transition between each upper and lower pair of adiabatic states, for each initial state of internuclear motion and all possible final motions, and summing these weighted by the rate of initial collisional motions. However, such calculations are only necessary to elucidate particular quantum features, because the *classical oscillator approximation*, *impact approximation, quasistatic approximation*, and *classical Franck–Condon principle* provide major conceptual and calculational simplifications. These are presented in the context of free–free transitions in the following sections.

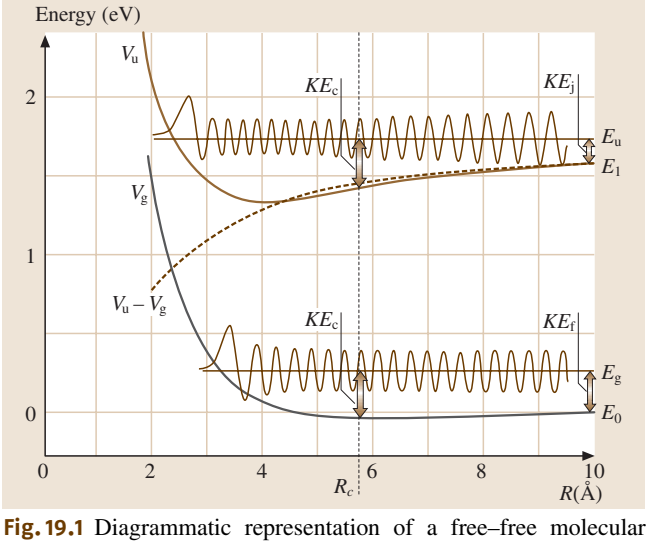

Fig. 19.1 Diagrammatic representation of a free–free molecular radiative transition and the classical Franck–Condon principle. Adiabatic potentials (V_u and V_g), the difference potential equal to the classical transition frequency (*dashed*), nuclear kinetic energies and wave functions $\Phi_u(R)$ and $\Phi_g(R)$ are indicated. The position R_C is the classical radiation position for the initial (E_u) and final (E_g) energies shown

19.1.3 Classical Oscillator Approximation

Consider a free–free molecular radiative transition of energy $\hbar\omega = E_u - E_g$ between upper (u) and lower (g) states of total energy E_u and E_g, as shown in Fig. 19.1. Each elastic scattering state is the product of an electronic adiabatic state $\phi(r, R)$ and a nuclear motion state $\Phi(R)$ of the molecule. The electronic states u and g have effective potentials

$$V_q^e = V_q + l(l+1)/R^2 \,, \qquad (19.1)$$

where $q = u$ or g. Examples of such $V(R)$ and $\Phi(R)$ for the case of $l = 0$ are shown in Fig. 19.1. The electric dipole radiation operator that couples these states is normally a weak perturbation that does not alter these potentials or wave functions. For definiteness assume the atom is initially in the upper state, and that an atom pair approach with kinetic energy $\mathcal{T}_i$ and separate with $\mathcal{T}_f$, as indicated. The intensity I, or transition probability, is proportional to the squared matrix element of the dipole operator $\boldsymbol{er} = e\Sigma_i \boldsymbol{r}_i$ between initial and final

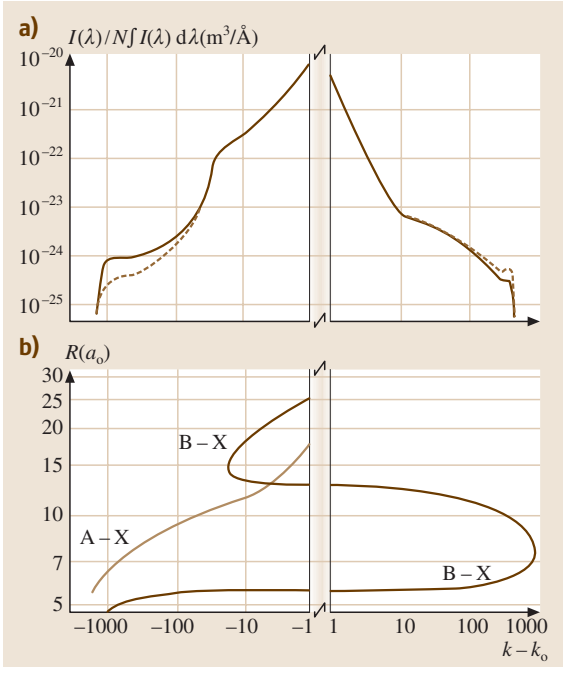

Fig. 19.3a,b Normalized intensity in the wings of the Rb $5P_{3/2} - 5S_{1/2}$ transition broadened by Kr, in frequency units of $k = 1/\lambda$. The measured spectrum in **(a)** is from [19.25–27]. The *solid line* is at 310 K and the *dashed line* at 540 K. The difference potentials corresponding to the A, B and X states of Rb – Kr, taken from [19.28], are shown in **(b)**

attributed to a long range attractive V_u which dominates $V_u - V_g$.

For the lowest n_P shown in Fig. 19.2, a convolution with the Doppler, hyperfine and instrumental broadenings showed that the line is essentially a symmetric Lorentzian for $|\Delta k| < \Delta k_c$ [19.25]. However, at the highest density, the half-height point is beginning to fall outside of Δk_c; the impact approximation is marginally valid for describing the half width of the line at this density. Most early experiments were done at more than 10 times this density [19.12]; most of the line-core was at $|\Delta k| > \Delta k_c$ and describable by the static theory (Sect. 19.1.7) rather than the impact approximation. The impact approximation was also not valid under these conditions because collisions overlap in time. These very broad lines are well represented by the multiple-perturber, static theories that assume scalarly additive perturber interactions [19.5, 7]. This transition between an impact and quasistatic line core, and to multiple perturber interactions, occurs at lower pressures for transitions to higher states, as the interactions have a longer range. In addition, nearby intensity peaks or satellites often occur, and strongly affect the line as pressure increases. An example calculation, based on an interpretation of measured spectra [19.13], is shown in Fig. 19.4. This shows how a line with a satellite feature progressively broadens and finally blends with the satellite as n_P increases.

With the advent of saturated-absorption (Doppler free) spectroscopy, collisional line broadening can be measured at much lower densities, where $2\gamma_c \ll \Delta\omega_D$. In principle, this can allow measurement of line broadenings and shifts, although with a complication that affects the line shape; the same collisions that produce optical phase shifts also change the atomic velocity. These velocity changes have a minor effect outside the Doppler envelope where high pressure measurements are normally made, but they are quite important in saturated absorption line shapes. This affects primarily the low intensity wings of the line, so it does not prevent measuring the broadening and shift of the nearly Lorentzian core.

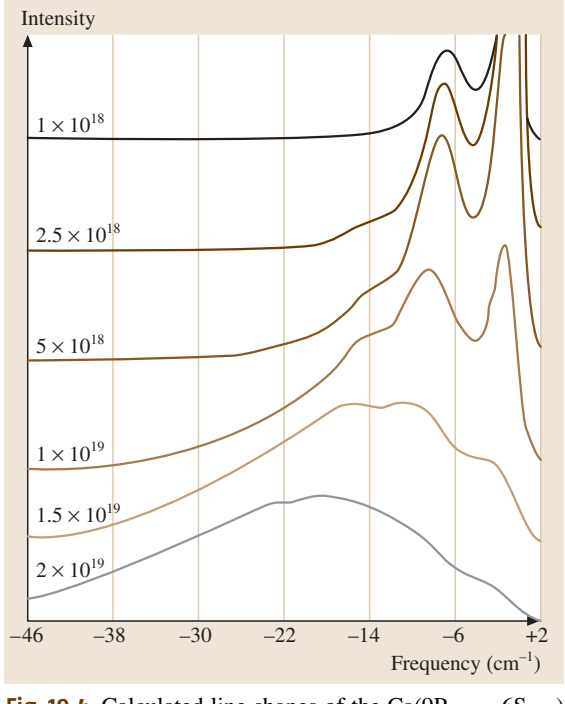

Fig. 19.4 Calculated line shapes of the $Cs(9P_{1/2} - 6S_{1/2})$ line broadened by Xe at the densities indicated (from [19.13]). The assumed interaction is based on measured line shapes, but data corresponding to the calculated conditions are not available

equilibrated internuclear motion sets

$$\frac{\mathrm{d}N_\mathrm{g}}{\mathrm{d}\omega} = N_\mathrm{g} n_\mathrm{P} 4\pi R^2 \frac{\mathrm{d}R}{\mathrm{d}\omega} \exp\left(-\frac{V_\mathrm{g}}{k_\mathrm{B}T}\right) , \qquad (19.12)$$

and equivalently for a radiating atom density N_u with perturber interaction V_u. Normally most of the radiation, and $\mathrm{d}N_\mathrm{g}/\mathrm{d}\omega$, is concentrated at the atomic line, so integrating over $\mathrm{d}\omega$ near the line leads to the relations

$$\int_0^\infty k(\omega)\,\mathrm{d}\omega = \frac{1}{2}\lambda^2 A_{21} N_\mathrm{g} \left(\frac{g_\mathrm{u}}{g_\mathrm{g}}\right) , \qquad (19.13)$$

$$\int_0^\infty I(\omega)\,\mathrm{d}\omega = A_{21} N_\mathrm{u} \left(\frac{h\omega}{2\pi}\right) , \text{ etc.} \qquad (19.14)$$

Note that

$$\frac{g(\omega)/N_\mathrm{u}}{k(\omega)/N_\mathrm{g}} \propto \exp\left(-\frac{\hbar\omega}{k_\mathrm{B}T}\right) ; \qquad (19.15)$$

if $N_\mathrm{u}/N_\mathrm{g}$ is also in equilibrium at T, this yields the correct equilibrium relation between $k(\omega)$, $g(\omega)$, $I(\omega)$, and a black body spectrum. While these relations are much more general than the QS theory, the latter provides a helpful conceptual basis. The above expressions in terms of spontaneous emission thus cover all cases.

19.2 Radiation Trapping

Atoms and ions efficiently absorb their own resonance radiation, and their emission can be reabsorbed before escaping a vapor. Molecules are less efficient absorbers, since each electronic transition branches into multiple-line bands, but interesting effects result if such reabsorption occurs. This emission and reabsorption process is fundamental to the formation of stellar lines, where it is called *radiation transfer*, and to confined vapors and plasmas where it is also called *radiation diffusion* or *trapping*. Fraunhofer's observation of dark lines in the stellar spectrum result from this radiation transfer process. Highly sophisticated treatments of line formation in inhomogeneous and nonequilibrium plasmas containing many species [19.15, 16] also apply to laboratory plasmas, but the simplifications inherent in a one- or two-element, confined plasma with cylindrical or planar symmetry leads to easier treatments. This sections discusses only a uniform density and temperature, confined atomic vapor.

The flourescent lamp in which 254 nm mercury radiation diffuses to the walls and excites a phosphor, provides a prime example of radiation trapping. Its improvement motivated the seminal *Biberman* [19.47] and *Holstein* [19.48] theories, continuing through modern theory and experiment that is particularly relevant to electrodeless and compact lamps. Dense clouds of cold, trapped atoms are also influenced by radiation trapping. Reference [19.49] provides and excellent overview of this topic, which we will not discuss here. The effect of radiation trapping on the *polarization* of flourescent radiation played a major role in developing a correct understanding of the coherent response of atoms to radiation. This is reviewed in [19.40], and will not be covered here. *Molisch* and *Oehry* [19.50] have provided a detailed discussion of research on radiation transport up to 1998.

19.2.1 Holstein–Biberman Theory

An atom in a dense vapor may be excited by externally applied radiation plus the fluorescence from other excited atoms within the vapor, and it will decay by spontaneous emission (neglecting stimulated emission). This is expressed by the Holstein–Biberman equation

$$\mathrm{d}n(\boldsymbol{r},t)/\mathrm{d}t = S(\boldsymbol{r},t) + \gamma \int_\mathrm{vol} K(\boldsymbol{r}-\boldsymbol{r}')n(\boldsymbol{r}',t)\,\mathrm{d}^3\boldsymbol{r}' - \gamma n(\boldsymbol{r},t) , \qquad (19.16)$$

where $n(\boldsymbol{r},t)$ is the excited state density at position $\boldsymbol{r}$, $S(\boldsymbol{r},t)$ is the excitation rate due to externally applied radiation, γ is the spontaneous emission rate, the kernel $K(\boldsymbol{r}-\boldsymbol{r}')$ is the probability of a reabsorption at $\boldsymbol{r}$ due to fluorescence by an atom at $\boldsymbol{r}'$, and the integral is over the vapor filled volume [19.47,48]. Since $K(\boldsymbol{r},\boldsymbol{r}')$ is assumed the same for all excited atoms, this contains an implicit assumption that all atoms emit the same fully redistributed spectrum. The solution of this linear integral equation, subject to boundary values at the vapor boundary, can be expressed as a sum over an orthogonal set of solutions $n(\boldsymbol{r},t)_i = n(\boldsymbol{r})_i \exp(-g_i\gamma t)$ of the homogeneous equation

$$n(\boldsymbol{r},t) = \sum_{i=1}^{\infty} a(t)_i n(\boldsymbol{r})_i , \qquad (19.17)$$

where, if $S(\boldsymbol{r},t)=S(\boldsymbol{r})f(t)$, then $a(t)_i=\bar{a}_i\int_{-\infty}^{t}f(t')\times\exp[-g_i\gamma(t-t')]\,\mathrm{d}t'$ and $\bar{a}_i=\int S(\boldsymbol{r})n(\boldsymbol{r})_i\,\mathrm{d}^3\boldsymbol{r}$. Here $n(\boldsymbol{r},t)_i$ is the ith normal mode and $g_i\gamma$ is the decay rate of this mode, as it would decay without change in its shape $n(\boldsymbol{r})_i$ from a pulse of excitation.

Two shapes of vapor regions have been studied in detail: an infinitely long cylinder of radius R and the region between two infinite parallel plates with separation L. The first three symmetric modes of the latter slab geometry are shown with unit height in Fig. 19.5. A spatial integration over the normalized $i=1$ or fundamental mode yields 1 and all others integrate to zero, so $a(t)_1$ equals the total excited state population. g_1 is the escape probability; i. e., the probability of photon escape averaged over the fundamental mode distribution of emitters $n(\boldsymbol{r})_1$. Since $n(\boldsymbol{r},t)$ must be everywhere positive, the negative contributions of the higher order modes only reduce the density in some regions. The g_i can vary from 0 to 1 and increase with increasing i, so that higher order modes die out faster after pulsed excitation. The ratios of decay rates is $g_i:g_3:g_5=1:3.7:6.4$ for the symmetric slab modes shown in Fig. 19.5. For steady state excitation, (19.17) yields $a(t)_i=\bar{a}_i/g_i\gamma$, so the lower order modes are more heavily weighted because they decay more slowly. The fundamental mode decay rate $g_1\gamma$ is of primary interest in most situations, and we will now discuss its properties.

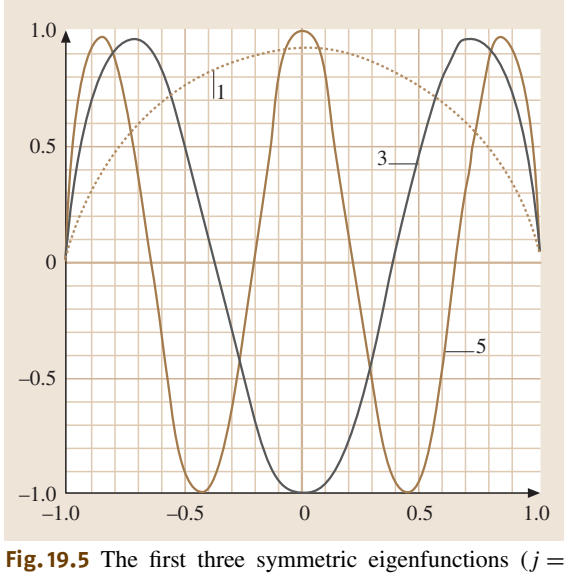

Fig. 19.5 The first three symmetric eigenfunctions ($j=0.2,4$) of radiation trapping between slab windows, for a Doppler line profile, from [19.51]. The windows are at ±1

The kernel $K(x)$ is the probability of fluorescence transport over a distance x followed by reabsorption, averaged over the emitted frequency distribution. It is conceptually useful to express it in terms of the spectrally averaged transmission $T(x)$

$$K(x)=\frac{1}{4\pi x^2}\frac{\mathrm{d}T(x)}{\mathrm{d}x}\,, \tag{19.18}$$

$$T(x)=\int_0^\infty \mathcal{L}(\omega)\exp[-k(\omega)x]\,\mathrm{d}\omega\,,$$

where $\mathcal{L}(\omega)$ is the emission line shape normalized to unit area, and $x=|\boldsymbol{r}-\boldsymbol{r}'|$. If one assumes that the fluorescence frequency of an atom does not depend on the frequency it absorbed (i. e., complete spectral redistribution), this leads to $k(\omega)=\kappa\mathcal{L}(\omega)$, where $\kappa=(\lambda^2/8\pi)(g_\mathrm{u}/g_\mathrm{g})n\Gamma$ and g_u and g_g are statistical weights. This simplification applies under most conditions and will be used here; its range of validity and more accurate treatments are discussed below.

The transmission factor $\mathcal{L}(\omega)$ and the integrand of (19.18) are shown in Fig. 19.6, for a Gaussian line shape and several values of k_0x, where k_0 is the line center absorption coefficient. At small k_0x, the transmitted spectrum is similar to $\mathcal{L}(\omega)$; for these conditions $T(x)\simeq\exp(-k_\mathrm{av}x)$, where $k_\mathrm{av}\simeq0.7k_0$ is the average attenuation. For $k_0x>5$, the transmission is small except at the edges of the line. The transmitted radiation is then predominately in the ω region near ω_1, defined by $k_0x\mathcal{L}(\omega_1)=1$. Since the integrand is sharply peaked near ω_1, this leads to simple analytic forms for $T(x)$. In

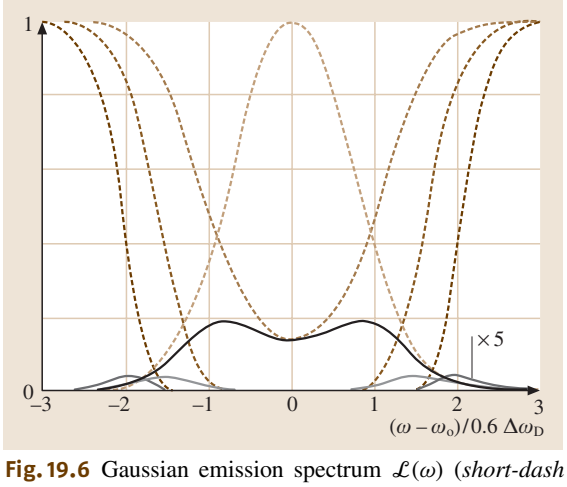

Fig. 19.6 Gaussian emission spectrum $\mathcal{L}(\omega)$ (*short-dash line*), transmissions $T(\omega)$ (*long-dash lines*), and transmitted intensities (*solid lines*) for $k_0x=2$, 10, and 50

broadening is due to a buffer gas, $\gamma_c = k_c n_B$ in (19.19b) yields

$$g_1 \propto \left(\frac{n_B}{n}\right)^{1/2}; \tag{19.20}$$

this has been studied in [19.56].

Post et al. have numerically evaluated g_1 for all values of $k_0 L$ for slab and cylinder geometries, by integrating the radiative escape probability $g(z)$ over the fundamental mode distribution $N(z)$, where z is the position between the windows [19.57]. To obtain $g(z)$ they integrate over the angular distribution of the emission, using $T(x)$ from the exact line shape. Thus all features of the calculation correspond to the Holstein–Biberman theory for an isolated line without approximation. As will now be discussed real atomic vapors are generally not that simple.

Many atomic "lines" have multiple components due to hyperfine structure and isotope shifts; some components are isolated while others are separated by less than a Doppler line width and overlap. The absorption line shape then becomes a weighted sum over components, each with an equivalent Voigt shape. In a high density vapor or a plasma, collisions will usually distribute the excited state population between the isotopes and hyperfine states in proportion to their isotopic fraction and statistical weight. The emission line shape $\mathcal{L}(\omega)$ is then a similarly weighted distribution over components. Since radiation only escapes in the wings of a line component at high $k_0 L$, overlapping components act almost as a single component. If the line has M isolated components, the right-hand side of (19.19a) and (19.19b) become sums over the fraction f_j of the intensity in the j component times the escape probability for that component. The latter is obtained, for large $k_0 L$, by replacing k_0 with $k_0 f_j$ in (19.19a) and (19.19b). The net result, after summing over components, is an increase in g_i by a factor of $\approx M$ in the Gaussian case and $\approx M^{1/2}$ in the Lorentzian. This approximation was obtained by Holstein in the context of the Hg 254 nm radiation under conditions appropriate to the fluorescent lamp [19.58]. Walsh made a more detailed study of these overlapping components [19.59], and the dependence of g_1 on the ratio of line separation to Doppler width is also given in [19.55].

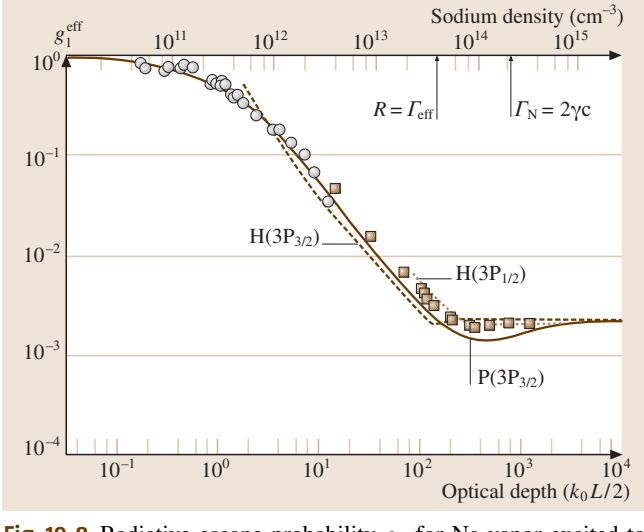

Fig. 19.8 Radiative escape probability g_1 for Na vapor excited to the $3P_{3/2}$ state, for a slab geometry. The Holstein approximation for the $3P_{3/2} - 3S_{1/2}$ (D2) line and the $3P_{1/2} - 3S_{1/2}$ (D1) line are indicated as *dashed lines*. The Post-type calculation of [19.53] for the D2 line is indicated as a *solid line*. *Solid squares* are data from [19.54], and *open circles* are data from [19.55]. The effective escape probability corresponds to the D2 line rate at low densities but a combination of D1 and D2 at high densities

19.2.3 Measurements

The overall behavior of g_1 versus n is shown in Fig. 19.8 for the Na($3P_{3/2}$) or D2 resonance line in pure Na vapor [19.54, 55]. In this type of experiment the fundamental mode decay rate is established by a combination of optimally exciting that spatial mode and of waiting until the fluorescence decay is exponential in time after termination of the excitation. A transition to approximately $1/n$ behavior, corresponding to (19.19a), is seen to occur at $k_0 L/2 \approx 5$. At $k_0 L/2 \approx 100$ the transition to n^0 behavior, corresponding to a self-broadened Lorentzian line in (19.19b), can be seen. The behavior at $k_0 L < 5$ fits the Milne diffusion theory [19.60] as well as the Post et al. theory shown as a solid line; this is also similar to $T(L/2)$, as seen in Fig. 19.7. For $5 < k_0 L/2 < 100$, the behavior is similar to (19.19a) (dashed line), but the Post et al. theory (solid line) is $\approx 20\%$ higher due to the inclusion of the Na hyperfine structure (hfs splitting $\simeq$ Doppler width). For $k_0 L/2 > 1000$, the Post theory converges to the Holstein–Lorentzian-line result with $\Gamma_{\text{Total}} = 2\gamma_c$.

The experiment is complicated in the $50 < k_0 L/2 < 500$ region by fine structure mixing [19.54]. The $3P_{3/2}$ state was excited, but at high densities, collisions populate the $3P_{1/2}$ state, which has a smaller g_1 than the $3P_{3/2}$ state (Fig. 19.8). At low densities, $g_1^{\text{eff}} = g_1(3P_{3/2})$, and at high densities these states are statistically populated

http://www.springer.com/978-0-387-20802-2

Springer Handbook of Atomic, Molecular, and Optical Physics
Drake, G. (Ed.)
2006, LVIII, 1506 p. 288 illus. in color. With CD-ROM.,
Hardcover
ISBN: 978-0-387-20802-2